Ras-dependent activation of BMAL2 regulates hypoxic metabolism in pancreatic cancer

H. Carlo Maurer[1*], Alvaro Curiel-Garcia[2,3*], Sam Holmstrom[4], Pasquale Laise[5, 6], Carmine F. Palermo[2,3], Steven A. Sastra[2,3], Anthony Andren[7], Zhang Li[7], Tessa LeLarge[8], Irina Sagalovskiy[2,3], Daniel R. Ross[2,3], Vilma Rosario[9], Kate Lu[10], Ethan Ferraiuolo[10], Nicholas Spinosa[10], Winston Wong[2], Kaitlin Shaw[11], John A. Chabot[12], Jeanine Genkinger[2,13], Hanina Hibshoosh[14], Gulam A. Manji[2,3], Alina Iuga[15], Roland M. Schmid[1], Michael A. Badgley[2,3], Kristen Johnson[10], Andrea Califano[2, 5,6], Costas Lyssiotis[7] , Kenneth P. Olive[2,3,†]

[1] Department of Internal Medicine II, Klinikum Rechts der Isar, School of Medicine, Technical University of Munich, 81675 Munich, Germany.
[2] Herbert Irving Comprehensive Cancer Center, Columbia University Irving Medical Center, New York, NY
[3] Department of Medicine, Vagelos College of Physicians and Surgeons, Columbia University, New York, NY
[4] UT Southwestern Medical Center, internal Medicine
[5] Department of Systems Biology, Vagelos College of Physicians and Surgeons, Columbia University, New York, NY
[6] Darwin Therapeutics, New York, NY
[7] Department of Internal Medicine, Division of Gastroenterology, University of Michigan, Ann Arbor, MI
[8] Department of Surgery, Dijklander Ziekenhuis Location Hoorn, Hoorn, the Netherlands
[9] Department of Surgery, Vagelos College of Physicians and Surgeons, Columbia University, New York, NY
[10] University of New Hampshire, Manchester, NH
[11] Columbia University Division of GI & Endocrine Surgery, Columbia University, New York, NY
[12] Department of Surgery, Vagelos College of Physicians and Surgeons, Columbia University, New York, NY
[13] Columbia University Mailman School of Public Health, New York, NY
[14] Department of Pathology and Cell Biology and HICCC, Columbia University, New York, NY
[15] University of North Carolina, Chapel Hill, NC
*These authors contributed equally.

Summary

To identify novel drivers of malignancy in pancreatic ductal adenocarcinoma (PDAC), we employed regulatory network analysis, which calculates the activity of transcription factors and other regulatory proteins based on the integrated expression of their positive and negative target genes. We generated a regulatory network for the malignant epithelial cells of human PDAC using gene expression data from a set of 197 laser capture microdissected human PDAC samples and 45 low-grade precursors, for which we had matched histopathological, clinical, and epidemiological annotation. We then identified the most highly activated and repressed regulatory proteins (e.g. master regulators or MRs) associated with four malignancy phenotypes: precursors vs. PDAC (initiation), low-grade vs. high grade histopathology (progression), survival post resection, and association with KRAS activity. Integrating across these phenotypes, the top MR of PDAC malignancy was found to be BMAL2, a member of the PAS family of bHLH transcription factors. Although the canonical function of BMAL2 is linked to the circadian rhythm protein CLOCK, annotation of BMAL2 target genes highlighted a potential role in hypoxia response. We previously demonstrated that PDAC is hypovascularized and hypoperfused, and here show that PDAC from the genetically engineered KPC model exists in a state of extreme hypoxia, with a partial oxygen pressure of <1mmHg. Given the close homology of BMAL2 to HIF1β (ARNT) and its potential to heterodimerize with HIF1A and HIF2A, we investigated whether BMAL2 plays a role in the hypoxic response of PDAC. Indeed, BMAL2 controlled numerous hypoxia response

genes and could be inhibited following treatment with multiple RAF, MEK, and ERK inhibitors, validating its association with RAS activity. Knockout of BMAL2 in four human PDAC cell lines led to defects in growth and invasion in the setting of hypoxia. Strikingly, BMAL2 null cells failed to induce glycolysis upon exposure to severe hypoxia and this was associated with a loss of expression of the glycolytic enzyme LDHA. Moreover, HIF1A was no longer stabilized under hypoxia in BMAL2 knockout cells. By contrast, HIF2A was hyper-stabilized under hypoxia, indicating a dysregulation of hypoxia metabolism in response to BMAL2 loss. We conclude that BMAL2 is a master regulator of hypoxic metabolism in PDAC, serving as a molecular switch between the disparate metabolic roles of HIF1A- and HIF2A-dependent hypoxia responses.

Statement of Significance

There is a surprising disconnect between the genomic alterations present in pancreatic ductal adenocarcinoma and key phenotypes of malignancy, suggesting that non-genetic factors must play a role. Here we analyze changes in regulatory state – calculated from network analysis of RNA expression data – to identify transcription factors and other regulatory proteins whose activities drive pancreatic cancer malignancy. We identified the top candidate, BMAL2, as a novel, KRAS-responsive regulator of hypoxic response in pancreatic cancer, serving as a switch between HIF1A and HIF2A expression. These data help explain how KRAS coordinates cell regulatory state to enable tumor cells to survive extreme hypoxia, and highlight the ability of regulatory network analysis to identify overlooked, key drivers of biological phenotypes.

Introduction

DNA sequencing of hundreds of human pancreatic tumors has helped define the genetic drivers of pancreatic ductal adenocarcinoma (PDAC). However, mutations poorly predict key, clinically relevant traits of the disease, such as tumor stage or therapeutic response [1, 2]. This suggests that non-genetic factors may control vital, biological characteristics of PDAC (differentiation state, metastatic potential, progression rate, etc.). Defining these factors will yield an improved understanding of the biological mechanisms that drive this devastating disease.

While RNA sequencing (RNA-Seq) has classically been used to study gene expression at the level of individual genes, new techniques in systems biology allow us to leverage the relationships *between* genes in a dataset to infer mechanistic drivers of phenotypes [3]. Briefly, the activity of transcription factors and other transcriptional regulators (collectively, “regulatory proteins” or RPs)

can be calculated from the integrated expression of their target genes using algorithms such as VIPER [4, 5]. By calculating the RPs whose activities are most hyperactivated or hyperrepressed between two phenotypes, one can determine the master transcriptional regulators (MRs) that drive the phenotype, and which are increasingly emerging as alternative therapeutic targets [3]. This approach is founded on algorithms such as ARACNe that can accurately infer context-specific sets of targets genes for each RP in the genome using largescale expression data [6-8].

Activating mutations in KRAS drive nearly all human PDAC tumors and extensive work has delineated the signal transduction pathways that effect its activity. However, the downstream transcriptional mediators of mutant KRAS in PDAC remain poorly understood. We set out to understand how mutant KRAS drives malignant phenotypes in PDAC.

Results

Master Regulator analysis of PDAC nominates BMAL2 as a PDAC driver

To study transcriptional regulatory changes that govern key phenotypes in PDAC, first we augmented our previous collection [9] of RNA samples derived from the malignant epithelium of laser-captured, microdissected (LCM) human PDAC to now include benign precursors and additional cancer samples. Termed the CUMC-E cohort, this sample set totals 197 PDAC, 26 low-grade pancreatic intraepithelial neoplasms (PanINs), and 19 low-grade intraductal papillary mucinous neoplasms (IPMNs) [10]. Here, low-grade PanIN and IPMN samples served as “benign controls” that are committed to the neoplastic lineage [11, 12] and yet unlikely to ever progress to PDAC [10, 13]. Indeed, unsupervised clustering (t-SNE) showed a clear distinction between precursor and PDAC expression profiles (**Figure 1A**).

Unbiased analysis of variance in gene expression revealed strong associations with histopathological features as observed in adjacent tissue sections (**Supplementary Figure S1A**). Expression of established markers of PDAC biology were also associated with histology, including KRAS [14-16], proliferation markers (TOP2A, BUB1B, CDC20, and TK1) [17], and indicators of squamous PDAC lineage (KRT5, KRT6A, PTHLH, and S100A2) [18, 19], which were highest among poorly differentiated tumors (**Figure 1B**). Conversely, hallmarks of differentiation (MUC1, MUC5AC) and GI lineage (TFF1, TFF2) decreased during tumor initiation and progression.

In order to quantify the activities of regulatory proteins in the CUMC-E dataset, we first applied ARACNe [4, 5] to the full set of 242 epithelial expression profiles, reverse-engineering a genome-

wide regulatory network model of PDAC epithelia. This compiled 263,085 inferred transcriptional targets for 2,211 regulatory proteins (RP). For 26 of these RPs, public ChIPSeq data were available in human PDAC cells [20]. Half of these (13/26) showed a significant overlap with the ARACNe target genes sets, depite the difference of *in vivo* versus cell cuture contexts (**Supplementary Figure S1B**), providing experimental validation for the regulatory network. Finally, in order to benchmark the regulatory network to established PDAC biology, we examined the inferred activities of proteins with well-established roles in pancreatic cancer (**Figure 1C**). Principal component 1 (PC1) captured a progression from benign precursors through low-grade PDAC, to high-grade PDAC with squamous features. These phenotypic changes were accompanied by repression of the canonical PDAC tumor suppressing transcription factors TP53 and SMAD4. The GI transcription factors GATA6, FOXA2, and PDX1, which have been described as being "overexpressed" in some PDAC molecular subtypes [15, 21], were down-regulated in PDAC relative to benign precursors, consistent with an overall loss of GI identity during tumor initiation and progression[15, 21]. These changes in tumor suppressor RPs were attended by steady increases in the activity of RPs with known oncogenic functions, such as FOXA1 [22] and TRIM29 [23] (**Figure 1C**) as well as other less well-known proteins. Finally, drivers of squamous histology such as TP63 [18] and ZBED2 [24] were hyperactivated in high-grade PDAC, particularly those with annotated squamous histology.

We next used the PDAC epithelial regulatory network in conjunction with inferred protein activity to identify regulatory proteins whose activities are associate with each of four key malignant phenotypes: tumor initiation, histological progression, reduced survival, and KRAS activity (**Supplementary Figure 1C)** [25, 26]. MARINa analysis identified MRs of PDAC initiation (comparing precursor to PDAC, **Figure 1D**) and progression (comparing PDAC with low-grade versus high-grade histology, **Figure 1E**). For survival, we constructed a survival signature from a multi-variate cox proportional hazards model and identified RP controlling the expression of the most prognostic target genes (**Figure 1F**). Interestingly, using overlap analysis, we found that the top survival MR proteins were associated with processes such as hypoxia, KRAS signaling, immune signaling, and EMT, but not proliferation (**Supplementary Figure S1D)**, suggesting that differences in the survival of PDAC patients are more complex than mere proliferative signaling [27].

Finally, to calculate KRAS activity, we iterated a new PDAC regulatory network comprising downstream signatures reporting the activity of 2,523 signaling factors (see Methods). In this analysis, the inferred target genes of each signaling protein serve as a bespoke reporter gene

set, providing an indirect, but unbiased, measure of its signaling activity in PDAC [7, 28]. As expected, the inferred activity of KRAS increased significantly during tumor initiation and tumor progression (**Supplementary Figure 1E**, $p < 0.001$, pairwise Welch's t-test with Bonferroni p-value adjustment), peaking among tumors growing in solid nests. Of all the RPs studied, BMAL2 activity exhibited the strongest association with KRAS signaling activity (rho = 0.86, **Figure 1E**). Integrating the MR results from all four malignancy phenotypes (initiation, histopathological progression, survival, and KRAS activity), we find that BMAL2 ranks as the top candidate master transcriptional regulator of PDAC malignancy (**Figure 1H**).

BMAL2 is associated with aggressiveness in multiple PDAC datasets

We next assessed the reproducibility of our findings by examining BMAL2 activity in multiple external datasets. We performed a meta-analysis across a total of 10 published PDAC expression studies [21, 29-37] and found that BMAL2 expression was elevated relative to normal pancreas (**Supplementary Figure S2A**) and in high-grade tumors versus low-grade PDAC specimen (**Supplementary Figure S2B**). Concordant with our findings in the CUMC cohort, high BMAL2 activity consistently identified patients with worse outcomes while its expression performed more variably (**Supplementary Figure S2C**). Finally, we evaluated each combination of five subtype classification schemes and six PDAC expression data sets for differences in BMAL2 activity between tumors of the most aggressive versus least aggressive subtype (**Supplementary Figure S2D**), and found that BMAL2 was consistently hyperactivated in the most aggressive subtype [38-40].

To learn more about possible lineage-specific patterns of BMAL2 expression we leveraged public resources from normal tissues [38], primary tumors [39] and cancer cell lines [40]. In normal tissues, BMAL2 expression was highest in those containing squamous epithelial cells, such as vagina, skin, and esophagus; expression in the normal pancreas was comparatively low (**Supplementary Figure S2E**). However, among human tumors from TCGA, PDAC exhibits the 6th highest level of BMAL2 expression, surpassed only by other squamous epithelial cancers (**Supplementary Fig. S2F**). Among 1304 cancer cell lines from the CCLE database, pancreatic cancer cells exhibited the highest median expression levels of BMAL2 (**Supplementary Figure S2G**).

KRAS signaling modulates BMAL2 activity

Our initial MR analysis showed that KRAS activity correlated closely with BMAL2 activity. To validate the relationship using experimental data, we identified published expression datasets in which mutant Kras activity was experimentally manipulated: $Kras^{G12D}$ reactivation in PDAC cells that survived Kras withdrawal (Viale); $Kras^{G12D}$ activation in murine pancreatic ductal cells (Sivakumar); and mutant Kras inactivation in murine and human PDAC cells (Ying, Bryant) [41-44]. In all four independent experiments, the BMAL2 activity was associated with Kras activation, raising the possibility that BMAL2 may contribute to transcriptional programs downstream of oncogenic KRAS (**Figure 2A**).

To further dissect the pathways that regulate BMAL2, we leveraged results from a recent analysis that presented high throughput RNA-Seq data from cell lines treated with 322 different FDA approved or investigational agents [45, 46] (**Figure 2B**). Using this approach, we identified drugs that were most capable of reducing BMAL2 activity in both cell lines tested (**Figure 2C**) and found a strong overrepresentation of MEK inhibitors, including trametinib, binimetinib, and refametinib. By contrast, we did not observe effects of this magnitude for inhibitors of other KRAS effector proteins, including PI3K, AKT, MTOR (**Figure 2D**). Although this screen lacked ERK inhibitors, a reanalysis of experimental expression data from PDAC cells treated with the ERK1/ERK2-selective inhibitor SCH772984 found decreasing BMAL2 activity over the course of 24 hours [44] (**Figure 2E**). Together, these findings suggest that BMAL2 receives input from oncogenic KRAS via the RAF/MEK/ERK effector pathway.

BMAL2 is a key regulator of the hypoxic response in pancreatic cancer

While our data suggested that mutant KRAS signaling can control BMAL2 activity, the phenotypic consequences of this regulation were unclear. Structurally, BMAL2 is related to ARNT, the binding partner of stabilized HIF1A, which is the predominant regulator of transcriptional responses to hypoxia in cells. Recent studies have shown that mutant KRAS expression enhances the hypoxic induction of HIF1A [47]. Based on our prior work showing that PDAC is hypovascular and hypoperfused [48], we tested whether autochthonous mouse pancreatic tumors are also hypoxic. We utilized an oxylite sensor (a gold-standard, physical oxygen probe) to measure the partial oxygen pressure (pO2) in the pancreatic tumors of $Kras^{LSL.G12D/+}$; $Trp53^{R172H/+}$; $Pdx1Cre^{tg/+}$ (KPC) mice. On average, pO_2 levels were <1mmHg in these tumors, indicating that PDAC cells exist in a state of extreme hypoxia (**Figure 3A**). Given the extraordinarily low oxygen present in these tumors and the fact that BMAL2 interacts with both HIF1A [49] and EPAS1 (HIF2α) [50], we hypothesized that BMAL2 could be exerting its effects through regulating responses to hypoxia.

To explore this possibility, we assessed whether BMAL2 could directly or indirectly regulate genes from a commonly-used hypoxia signature [51]. To do this, we both the sets of target genes directly regulated by BMAL2 as well as the sets of target genes regulated by each RP regulated by BMAL2 through one or two degrees of connection. Strikingly, this analysis found that BMAL2 regulates 33 out of 44 hypoxia genes in a net positive manner, including metabolic proteins such as SLC2A1 (GLUT1), GAPDH and LDHA (**Figure 3B**). None of the hypoxia genes were regulated in a net negative manner. This prompted us investigate BMAL2's function under both normoxic (21% O_2) and hypoxic (1% O_2) conditions in greater detail by loss-of-function analyses in PDAC cell lines (**Figure 3B**). We found that cells lacking functional BMAL2 exhibited reduced cell proliferation (**Figure 3C**). Similarly, cell migration was impaired upon BMAL2 loss of function, specifically under hypoxic conditions (**Figure 3D**). Higher media pH (**Figure 3E**) and a blunted lactate response to hypoxia (**Figure 3E**) in BMAL2 knockout cells suggested an impaired metabolic adaption to hypoxia. Additionally, we found BMAL2 knockout cells failed to stabilize HIF1A under hypoxic conditions (**Figure 3G**) and could confirm a decrease in LDHA and GAPDH protein levels in BMAL2 knockout cells, while EPAS1 (HIF2A) levels increased in response to BMAL2 knockout under hypoxic conditions, possibly indicating a shift in the hypoxia response from HIF1A to HIF2A-mediated hypoxia programs. We conclude that BMAL2 is a KRAS-responsive master regulator of the hypoxic response in PDAC.

Discussion

The conservation of genomic alterations between precursor lesions, primary and metastatic PDAC tumors [1, 2, 17] has centered our efforts to identify drivers of PDAC progression and dedifferentiation using epigenetic and transcriptional changes. Our study now allows for their unbiased investigation across multiple critical PDAC phenotypes at unprecedented scale using genome-wide context-specific regulatory network analysis.

Perhaps expected for laser-guided sample acquisition, we find transcriptional and histopathological dedifferentiation to be closely mirrored from low-grade precursor lesions to tumors growing in solid nests. One important observation from this dedifferentiation continuum concerns the role of transcriptional regulators of normal pancreatic development in PDAC carcinogenesis. For example, GATA6 has been ascribed oncogenic functions based on early observations of copy number gains in PDAC specimen [52, 53] and apparent "overexpression" in the classical PDAC subtype [15, 21]. However, more in-depth functional characterization [54, 55] pointed to a largely tumor-suppressive role and questions the rationale to target GATA6 and its gene program in PDAC. Consistent with these experiments, we find GATA6 to be among the

regulatory proteins exhibiting substantial loss of activity during both tumor initiation and progression. We find similar patterns of activity dysregulation for the majority of developmental pancreatic RP including PDX1, HNF1B, and SOX9, thereby questioning their role as “drivers” of low-grade, classical tumors. Based on these findings, we hypothesize that perturbation of these pancreatic RP anywhere along the progression continuum starting from low-grade precursors could induce further dedifferentiation and inadvertently worse patient outcome.

Furthermore, we have identified novel master regulators of PDAC malignancy and robust prognostic biomarkers of aggressive disease by integrating regulatory protein signatures from four critical phenotypes of PDAC carcinogenesis: initiation, progression, survival and KRAS response. In contrast to the developmental pancreatic RP mentioned above, we hypothesize that these genes may represent therapeutic targets that when antagonized will return pancreatic cancer cells on the progression and dedifferentiation continuum.

At the top of the candidate list stands BMAL2, also known as MOP9 and cycle like factor (CLIF), respectively, a member of the bHLH-PAS family of heterodimeric transcription factors that regulate biological responses to light, oxygen, and certain environmental pollutants [49, 50]. Under physiological conditions BMAL2 partners with CLOCK to bind to enhancer elements near genes regulated with circadian rhythmicity including the Plasminogen activator inhibitor-1 (SERPINE1). Furthermore, the Arnt2l/Clock heterodimer was shown to drive the expression of pro-metastatic secreted factors including Smoc2 in a murine lung cancer model [56].

BMAL2 levels were previously shown to indicate higher tumor aggressiveness in lung, colon and pancreatic cancer [56-58]. We have extended this analysis to a pancancer-level for BMAL2 mRNA and examined 6 further PDAC cohorts (n = 824 cases) at the expression and activity level. Using complementary statistical approaches, we found particularly high BMAL2 activity to be a robust marker of poor disease outcome.

BMAL2 is further found to correlate strongly with KRAS activation throughout PDAC carcinogenesis and is activated upon increased experimental KRAS function. Furthermore, in an unbiased assessment of drug mechanism of action across more than 300 antineoplastic compounds we identify inhibitors of canonical KRAS-MEK signaling to prevail among drugs reversing BMAL2’s gene program.

Our identification and subsequent functional characterization of BMAL2 integrates seamlessly with recent correlative observations of signatures reflecting increased KRAS signaling and hypoxia response during metastatic progression and tumor invasiveness [15, 17, 59].

Data Availability Statement

The data generated in this study are available upon request from the corresponding author.

Ethics Statement

All mouse studies performed were approved by the Columbia University Irving Medical Center (CUIMC) Institutional Animal Care and Use Committee (IACUC). All work using patient samples were performed with approval from the CUIMC Institutional Review Board (IRB).

Acknowledgmens

KPO and CAL were supported by the NCI (R01CA215607, R01CA244931). KPO also was supported by a Career Development Award from Pancreatic Cancer Action Network and a Clinical Translational Research Award from the Lustgarten Foundation for Pancreatic Cancer Research. ACG received support from the Charles H. Revson Senior Fellowship in Biomedical Science (Grant No. 22-22). KJ received research supported by New Hampshire- INBRE through an Institutional Development Award (IDeA), P20GM103506, from the National Institute of General Medical Sciences of the NIH. HCM received support from a Mildred Scheel Postdoctoral Fellowship (Deutsche Krebshilfe) and the KKF Clinician-Scientist program (TUM). This work utilized resources from the CU-DLDRC (P30 DK132710() and the Columbia University CCSG (5P30CA013696), including the Genomics, OPTIC, Database, Molecular Pathology Shared Rescources.

Declaration of interests

A.C. is founder, equity holder, consultant, and director of DarwinHealth Inc., which has licensed IP related to these algorithms from Columbia University. Columbia University is an equity holder in DarwinHealth Inc. P.L. is Sr. Director of Single-Cell Systems Pharmacology at DarwinHealth Inc, a company that has licensed some of the algorithms used in this manuscript from Columbia University.

Author's contributions

H.C.M. and K.P.O conceived the project. H.C.M. started the project and performed the LCM dataset and the computational analyses. A.C.G. designed, performed and oversaw the

experimental analyses and contributed to the computational analyses. S.H., P.L.,C.F.P, S.A.S, A.A.,Z.L.,T.L., I.S.,D.R.R., V.R., K.L., .F., N.S., W.W., K.S., J.A.C., J.G., H.H., contributed to experimental execution, data acquisition and data generation. A.I. reviewed histopathology for PDAC samples in the CUMC cohort. G.A.M. and W.W. aided in the curation of human outcomes data. H.C.M, A.C.G., M.A.B and K.P.O. wrote the manuscript with feedback and editing from R.M.S., M.A.B., K.J., A.C. and C.L.

Figure Legends

Figure 1. (**A**) Principal component analysis (PCA) of precursor and PDAC LCM RNA-Seq samples used to assemble a regulatory model (interactome) of PDAC carcinogenesis. (**B**) Heatmap depicting select differentially expressed genes between the indicated histopathological groups (x-axis). Wald test statistics were derived from a negative-binomial linear model comparing the respective group against all other groups. (**C**) Heatmap of protein activity scores (NES) for select RP during PDAC progression. The samples are ordered by their value in the first principal component, essentially capturing progression and dedifferentiation. (**D**) Select results from Master regulator analysis on a genome-wide PDAC initiation gene expression signature (x-axis) represented by Z-scores for each gene. Each regulatory protein's regulon is represented by red (positive targets) and blue (negative targets) vertical bars. The rank of each RP based on activity and expression, respectively, is illustrated on the right. (**E**) Select results from Master regulator analysis on a genome-wide PDAC progression gene expression signature (x-axis) (**F**) Select results from Master regulator analysis on a genome-wide survival signature (x-axis) represented by Wald test statistics from a multivariate Cox Proportional Hazards model accounting for age and each gene's continuous expression (**G**) Genome-wide Pearson correlation between KRAS and RP activity with illustration of the most positively correlated RPs (**H**) Heatmap of rank positions for the indicated regulatory proteins (x-axis) in each of four critical phenotypic PDAC transitions yields a conserved core set of non-oncogene dependency candidates for PDAC. A low rank represents activation in a given phenotype signature.

Figure 2. (A) BMAL2 regulon enrichment in the indicated genome-wide response gene expression signatures to oncogenic KRAS mutation. Positive and negative targets, respectively, are represented by red and blue vertical bars, respectively. Normalized enrichment score (NES) and p-values are calculated by two-tailed analytic rank-based enrichment analysis (aREA, p-values are Bonferroni corrected) **(B)** Schematic of the experimental design to study the effect of a library of antineoplastic compounds on regulatory protein activity as part of the OncoTreat

framework. **(C)** Effects of 322 antineoplastic compounds on BMAL2 activity (NES) in ASPC1 (x-axis) and PANC1 (y-axis) cells. Zoomed area focusses on compounds with consistent and potent reversal of BMAL2 activity. Red circles mark MEK inhibitors, all other compounds are grey. **(D)** Reversal of BMAL2 activity (y-axis, normalized enrichment score, NES) for the indicated compound classes (x-axis). P-values are derived from pairwise t-tests with posthoc Bonferroni correction. **(E)** Reversal of BMAL2 activity (y-axis, NES) at the indicated time points of treatment with an ERK inhibitor (SCH772984) in 7 PDAC cell lines. P-values are derived from one-sample, two-tailed t-tests with Bonferronic correction. **: $p \leq 0.01$, ***: $p \leq 0.001$, ns: not significant.

In boxplots, the box ranges from Q1 (the first quartile) to Q3 (the third quartile) of the distribution and the range represents the IQR (interquartile range). The median is indicated by a dashed line across the box. The “whiskers” on box plots extend from Q1 and Q3 to 1.5 times the IQR.

Figure 3. (**A**) Oxygen tension (y-axis) as determined by an OxyLite probe in tumors from KPC mice breathing ambient air or pure oxygen (x-axis). Dark blue circles represent averages per tumor and boxplots illustrate their distribution. Light blue circles represent repeat measurments per tumor. (**B**) HIF target genes (orange) controlled directly or indirectly by BMAL2 (yellow). Indirect control involves both BMAL2's negative influence on first (dark blue) or second tier (light blue) RP repressing HIF target genes, and positive influence on first (dark red) and second (light red) tier RP activating HIF target genes. (**C**) Fold change in cell growth relative to cells expressing non-targeting sgRNA in normoxic (21% O2) and hypoxic (1% O2) conditions (**D**) Number of migrated cells for cells expressing non-targeting or BMAL2-directed sgRNA in the indicated oxygen environment. P-values are derived from testing the indicated coefficients from a linear regression model. Significant interaction term suggests synergistic effects of BMAL2 pertubation and hypoxia on cell migration. (**E**) Media pH levels after 72 hours incubation. P-values derived from Welch's t-test (**F**) Fold change in lactate levels in the indicated oxygen environment expressing either non-targeting or BMAL2-directed sgRNA (**G**) Western Blot for HIF1a, HIF2a,

Methods

Patient population and samples generation

Patient population. Freshly frozen tissue samples were obtained from patients who underwent surgical resection at the Pancreas Center at Columbia University Medical Center as described previously [9]. The clinical data of these patients are shown in Supplementary Tables S1 and S2. Before surgery, all patients had given surgical informed consent, which was approved by the institutional review board. Immediately after surgical removal, the specimens were cryopreserved, sectioned, and microscopically evaluated by the Columbia University Tumor Bank (IRB AAAB2667). Suitable samples were transferred into OCT medium (Tissue Tek) and snap-frozen in a 2-methylbutane dry ice slurry. The tissue blocks were stored at -80°C until further processing. H&E stained sections of frozen PDAC samples from the Tumor Bank were initially screened to confirm the diagnosis and overall sample RNA quality was assessed by the Pancreas Center supported Next Generation Tumor Banking program using gel electrophoresis, with samples exhibiting high RNA quality utilized for subsequent analyses.

Laser Capture Microdissection (LCM), RNA sequencing, and gene expression quantification. LCM-RNA-Seq was performed as described previously [9, 60]. Briefly, Cryosections of OCT-embedded tissue blocks were transferred to PEN membrane glass slides and stained with cresyl violet acetate. Adjacent sections were H&E stained for pathology review. Laser capture microdissection was performed on a PALM MicroBeam microscope (Zeiss), collecting at least 1000 cells per compartment. RNA was extracted and libraries were prepared using the Ovation RNA-Seq System V2 kit (NuGEN). Libraries were sequenced to a depth of 30million, 100bp, single-end reads on an Illumina HiSeq 2000 platform. Reads and transcripts per million (TPM) were estimated for each transcript using the transcript sequences from the GENCODE Release 34 (GRCh38.p5) and the Salmon software (v1.3.0). Counts and TPM were summarized at the gene level by summing up the transcript values for each corresponding gene.

Computational methods

Assembly of a PDAC regulatory model and network analysis. A cell regulatory network for pancreatic carcinogenesis (CUMC-E interactome) was reverse-engineered by ARACNe-AP [5] using 242 epithelial LCM-RNA-Seq gene expression profiles. Genes with detection rates at 10 counts below 25% in all of the examined conditions (PanIN, IPMN, and PDAC) were removed and the variance was stabilized by fitting the dispersion to a negative binomial distribution as implemented in the DESeq2 R package [61]. ARACNe was run with standard settings (using data processing inequality (DPI), with 100 bootstrap iterations using human gene symbols mapping to

a set of 1665 transcription factors and 1025 transcription cofactors as described by AnimalTFDB 3.0 [62]. For the signaling network a set of 3370 signaling-pathway-related genes was considered which were annotated in the GO Biological Process database as GO:0007165—'signal transduction 'and in the GO Cellular Component database as GO:0005622—'intracellular 'or GO:0005886—'plasma membrane'. Thresholds for the tolerated DPI and mutual information P value were set to 0 and 10–8, respectively. Cytoscape v3.7.1 [63] was used to illustrate subnetworks of relevant regulatory proteins. Community detection was performed by using the fastgreedy.community [26] function in the *igraph* R package. The CUMC-E interactome is available as R object from https://doi.org/10.6084/m9.figshare.13160078.v2.

Master Regulator Analysis and inference of virtual protein activity. The enrichment of each regulatory protein regulon in the progression and dedifferentiation signature, respectively, was inferred by the MARINa algorithm as implemented in the *msviper* function from the *viper* R package [25, 28, 64]. Statistical significance was estimated by permuting the sample labels uniformly at random 1,000 times. For single-sample analysis including precursor and tumor samples, unsupervised gene expression signatures were computed by a z-score transformation of the variance-stabilized data. This was performed gene-by-gene, by first subtracting the mean expression level across all samples and then dividing by its standard deviation. Relative protein activity was then inferred for each sample with the VIPER algorithm. For a patient-based approach including the assessment of whether significant dysregulation of an individual regulatory protein occurs in a given tumor, single sample gene expression signatures were computed for each primary sample by subtracting the mean of all precursor samples (n = 45) and dividing by their standard deviation. RP activity was then inferred by VIPER analysis of each PDAC gene expression signature. P-values were estimated by the analytical approximation implemented in the aREA algorithm, which is virtually equivalent to estimations obtained by permuting the genes in the signature uniformly at random [28]. P-values were corrected to account for multiple hypothesis testing by the Benjamini-Hochberg method.

Gene set enrichment analysis and scoring. One-tail gene set enrichment analysis was implemented as described [65]. Two-tailed gene set enrichment analysis and enrichment of individual ARACNe regulons were carried out using analytic rank-based enrichment analysis (aREA) [28]. Functional annotation of ARACNe-derived regulons was carried out by testing the overrepresentation of HALLMARK gene sets (MSigDb v6.0) among all target genes of a given

regulatory protein with the gene universe set to all unique genes in the CUMC-E interactome (n=18658) using a two-tailed Fisher's Exact test.

Differential gene expression. Genome-wide differential gene expression analysis was generally calculated using the *DESeq2 [61]* R package for RNA-Seq count data and the *limma* R package [66] for microarray data. For comparisons including both RNA-Seq and microarray data, differential gene expression for count data was repeated using the *voom-limma* framework for the sake of consistency with the microarray analysis.

Survival signature and assessment of prognostic relevance. In an unbiased approach to study the association of gene expression and protein activity with patient outcome, a genome-wide survival signature was computed by fitting a multivariate Cox Proportional Hazards model (CPHM) accounting for the age at diagnosis and the continuous, normalized expression of a respective gene using the *survival* R package [67]. Next, we extracted the ensuing Wald statistic of the coefficient for gene expression with higher values corresponding to higher hazard ratios and vice versa and applied MARINa with a gene permutation null model to this survival signature to infer regulatory proteins controlling the survival signature.

Effect size meta-analysis. The effect size (i.e. $\log_2$ fold change) and its standard error for BMAL2 were extracted from the respective genome-wide differential expression analysis of a total of 10 studies where global expression in normal vs. primary tumors and low-grade vs. high-grade tumors, respectively, was contrasted. Similarly, the coefficient (log hazard ratio) and its standard error for the upper tertile of BMAL2 expression and activity, respectively, were extracted from a CPHM in cohorts with available time-to-event data. Meta-analysis was carried out using the *metafor* R package [68]. Both random and fixed effect models were fit using the *rma* function (method = "REML" and method = "FE").

Molecular subtyping. Moffitt classes were determined for 197 primary PDAC LCM-RNA-Seq profiles as described previously [29]. Briefly, using the 50 (47 with a unique match in our data) tumor-specific transcripts from Moffitt et al., we applied consensus clustering to our mRNA cohort with Euclidean distance and the partitioning around medoids (PAM) algorithm, seeking and reproducing two clusters of both genes and samples.

External data

Human PDAC cohorts. For the TCGA-PAAD cohort, raw count data were retrieved from the GDC Data portal for 149 patients described previously [35] and the variance was stabilized as described above. For the ICGC-PACA-AU cohort described previously [37], normalized gene expression data for 96 patients were provided by the authors in Suppl. Table 2. Microarray data of primary PDAC specimen from Collisson et al. [21] (n = 27), Moffitt et al. [29] (n = 252), and Puleo et al. [36] (n = 309) were retrieved from GSE17891, GSE71729 and E-MTAB-6134, respectively. Studies containing expression data from both normal pancreas and PDAC were processed and analyzed as described previously [69].

TCGA Pan-Cancer Atlas. Processed clinical and expression data were retrieved from the Genomic Data Commons Pan-Cancer homepage [70]. Information on sample types was added using TCGA sample barcodes. Only tumor samples were retained for expression level analysis and association of outcome with BMAL2 expression tertiles, respectively.

The Cancer Dependency Map. Processed genomic and perturbation data together with sample annotation were retrieved from the The Cancer Dependency Map Project website [16] (version Public 20Q4).

Gene perturbation signatures. Raw microarray data from a mouse model harboring a dox-inducible oncogenic $Kras^{G12D}$ were retrieved from GSE32277 [41] and GSE58307 [42] and processed using the *affy* and *gcrma* R packages. Processed Microarray data from normal murine ductal cells in which oncogenic $Kras^{G12D}$ was turned on using adenoviral Cre recombinase were retrieved from GSE89846 [43]. Raw RNA-Seq data from human PDAC cell lines stably transfected with shRNA targeting KRAS were retrieved from the European Nucleotide Archive under accession PRJEB25797 [44]. RNA-Seq counts were analyzed using the voom-limma framework implemented in the *edgeR* and *limma* R packages.

Experimental methods

Cell culture. PANC-1 and PaTu 8902 cell lines were obtained from ATCC and tested negative for mycoplasma infection. Cells were maintained under standard conditions at 37ºC and 5% CO_2. Cells were grown in DMEM (Life Technologies, 12430-054) supplemented with penicillin and streptomycin (Corning, 30-003-CI), 10% FBS (Life Technologies, 10438-034), and MEM NEAA (Life Technologies, 11140-050) unless otherwise indicated.

Genome editing and transfection protocol. The sgRNA (small-guide RNA) to knocking-out BMAL2 as well as non-targeting (NT) sequence were purchased from GenScript (Piscataway, NJ) using pLentiGuide-Puro vector as a backbone. PANC-1 cells were first infected with a

pLentiCas9-Blast vector (addgene, #52962) for a constitutive Cas9 expression and selected with Blasticidin (AG Scientific, #B-1247-SOL). Cells expressing Cas9 were then infected with selected virus (BMAL2/NT) using the lentiviral protocol according to the manufacturer's instructions.

Viability, lactate and migration assays. PaTu 8902 cells were seeded at $3x10^3$ cells per well in 96 well plates and incubated 12 hours either under normoxia or moved to the hypoxia chamber with 1% O_2(StemCell, #27310). After incubation time, lactate assay was performed using 5 μl of media and the luminometric Lactate-Glo assay kit (Promega, # J5021) according to the manufacturer protocol. To measure cell viability, Alamar Blue reagent (Bio-rad, # BUF012) was added to the culture media for 4 h, and absorbance was determined at 570 and 600 nm using a Varioskan LUX Multimode Microplate Reader (Thermo, #3020-80389). For migration assay, Panc1 cells carrying sgRNA-NT or sgRNA-BMAL2 were seeded (1×10^5) into a transwell membrane inserts in serum-free culture media (5 μm pore, Corning #3412) and regular media was added to the lower chamber. Cells were incubated for 24h in regular conditions. After the incubation time, plates were incubated either under normoxia (37°C, 5% CO_2, 20%O_2) or moved to the hypoxia chamber (37°C, 5% CO_2, 1%O_2) for 14 hours and cells that migrated across the membrane were fixed and stained with crystal violet and counted under the microscope.

pH assay: pH measurements were taken from media samples using Orion 9810BN Micro pH Electrode (Thermo Scientific, #9810BN) and the Orion 3-Star Benchtop pH Meter (Thermo Scientific, #111210). The micro electrode was calibrated using fresh standard buffers (Thermo Scientific, #910199) prior to all measurements. Measurements were taken by allowing the pH microprobe ample time to equilibrate in the media samples prior to recording the data. All pH calibrations and measurements were performed following the manufacturers protocol.

Immunoprecipitation and immunoblotting: Cell pellets were lysed with RIPA lysis buffer (Cell Signaling, #9806S) and protein concentrations were determined by BCA protein assay kit (Thermo Scientific, #23227) using the manufacture's protocol. Proteins were separated on Mini-PROTEAN TGX gels (Bio-Rad, #4561093) and transferred to nitrocellulose membrane (Bio-Rad, #1704156). Membranes were incubated in blocking buffer (5% BSA, 0.1% Tween-20, 10 mM Tris at pH 7.6, 100 mM NaCl) for 1 hour and then with primary antibody overnight at 4 C according to the antibody datasheet. Antibodies used: HIF1a (1:1000, Cell Signaling, #36169S), beta-Actin (1:1000, Cell Signaling, #4970S), HIF-2a (1:1000, Cell Signaling, #7096S), BMAL2 (1:500, Abcam, #ab221557), LDHA (1:1000, Cell Signaling, #3582S), GAPDH (1:1000, Cell Signaling, #2118S) and Tubulin (1:1000, Cell Signaling, #2146S). Anti-rabbit-HRP (Cell Signaling, #7074S) conjugated antibodies was used to detect desired protein by chemoluminescence with ECL (Bio-

Rad, #170-5061). For immunoprecipitation, lysate containing 1000 µg total protein was mixed with either 10 µl HIF1a antibody in a total volume of 500 µl using the Pierce™ BCA Protein Assay Kit and manufracturer instructions (Thermo Scientific™, cat. #23225, Waltham, MA). Samples were resuspended in 50 µl 2X Laemmli Sample Buffer and boiled for 10 min at 100 °C. Next, proteins were separated on a 15% SDS-PAGE gel and visualized with ECL (Bio-Rad, #170-5061).

RNA extraction and RNA sequencing. Total RNA from proliferation assays was extracted using trizol (Invitrogen) using the manufacturer 'protocol and the quality of the sample was analyzed using the 2100 bioanalyzer system (Agilent). Samples were then sequenced using Illumina NovaSeq.

KPC Mice. KrasLSL.G12D/+; p53LSL.R172H/+; Pdx1-Cre (KPC) mice were bred by crossing the KrasLSL.G12D, p53LSL.R172H, and Pdx1-Cre strains. Triple mutant mice were palpated twice weekly for evidence of early tumours beginning at 8 weeks of age, followed by subsequent B-mode ultrasound screening using a VisualSonics 2100 Vevo High Resolution System. Following detection, tumours were monitored once weekly until reaching a mean diameter of 6 mm.

Oxylite Measurements. Intratumoral partial oxygen pressures in KPC mice (n=16) were measured using the OxyliteTM fluorescence quenching-based system (Oxford Optronics). Tumour-bearing KPC mice were anesthetized with 2% isoflurane in either air or pure oxygen (as indicated). Hair was removed with depilatory cream around the abdomen and the tumour was visualized by ultrasound as above. A syringe with a 21G needle was attached to a stereotactic mount and inserted through the skin and abdominal wall. Real-time ultrasound imaging was used to visually guide the needle in-plane with the image through the centre of the tumour until reaching the far edge. With the needle in place, the syringe was carefully removed and the bare-fibre oxygen-sensing OxyliteTM probe was then attached to the stereotactic mount and threaded through the needle bore until the probe tip was localized at the far edge of the tumour. The needle was fully retracted over the fibre and an initial pO2 measurement was taken at the far site. Prior to each measurement, the probe was allowed to equilibrate for 3-5 minutes until readings stabilized. After the initial reading, the fibre was retracted incrementally through the needle track, with readings taken every 1-2 mm, through the full depth of the tumour (ranged from 6-12 mm in diameter). Measurements within 1 mm of the edge of the tumour were excluded from the analysis since the needle frequently punctured the far wall of the tumour, allowing oxygen from the abdominal cavity into the wound (as made apparent by a sharp spike in readings). To compare tumour to normal tissue, partial pressures were also measured in pancreas and kidney of WT mice (n=4) kept under anaesthesia using compressed air as vehicle. After completing

measurements, mice were euthanized by isoflurane overdose and tissue was harvested for formalin fixation for 24 h prior to paraffin embedding. All tumours were verified as pancreatic ductal adenocarcinoma by a blinded observer experienced in mouse tumour pathology.

References

1. Murphy, S.J., et al., *Genetic alterations associated with progression from pancreatic intraepithelial neoplasia to invasive pancreatic tumor.* Gastroenterology, 2013. **145**(5): p. 1098-1109.e1.
2. Makohon-Moore, A.P., et al., *Limited heterogeneity of known driver gene mutations among the metastases of individual patients with pancreatic cancer.* Nat. Genet., 2017. **49**(3): p. 358-366.
3. Califano, A. and M.J. Alvarez, *The recurrent architecture of tumour initiation, progression and drug sensitivity.* Nat. Rev. Cancer, 2017. **17**(2): p. 116-130.
4. Basso, K., et al., *Reverse engineering of regulatory networks in human B cells.* Nat. Genet., 2005. **37**(4): p. 382-390.
5. Lachmann, A., et al., *ARACNe-AP: gene network reverse engineering through adaptive partitioning inference of mutual information.* Bioinformatics, 2016. **32**(14): p. 2233-2235.
6. Aytes, A., et al., *Cross-species regulatory network analysis identifies a synergistic interaction between FOXM1 and CENPF that drives prostate cancer malignancy.* Cancer Cell, 2014. **25**(5): p. 638-651.
7. Piovan, E., et al., *Direct reversal of glucocorticoid resistance by AKT inhibition in acute lymphoblastic leukemia.* Cancer Cell, 2013. **24**(6): p. 766-776.
8. Carro, M.S., et al., *The transcriptional network for mesenchymal transformation of brain tumours.* Nature, 2010. **463**(7279): p. 318-325.
9. Maurer, C., et al., *Experimental microdissection enables functional harmonisation of pancreatic cancer subtypes.* Gut, 2019. **68**(6): p. 1034-1043.
10. Basturk, O., et al., *A Revised Classification System and Recommendations From the Baltimore Consensus Meeting for Neoplastic Precursor Lesions in the Pancreas.* Am. J. Surg. Pathol., 2015. **39**(12): p. 1730-1741.
11. Maitra, A. and S.D. Leach, *Disputed paternity: the uncertain ancestry of pancreatic ductal neoplasia.* Cancer Cell, 2012. **22**(6): p. 701-703.
12. Patra, K.C., N. Bardeesy, and Y. Mizukami, *Diversity of Precursor Lesions For Pancreatic Cancer: The Genetics and Biology of Intraductal Papillary Mucinous Neoplasm.* Clin. Transl. Gastroenterol., 2017. **8**(4): p. e86.

13. Matthaei, H., et al., *Presence of pancreatic intraepithelial neoplasia in the pancreatic transection margin does not influence outcome in patients with R0 resected pancreatic cancer.* Ann. Surg. Oncol., 2011. **18**(12): p. 3493-3499.
14. Mueller, S., et al., *Evolutionary routes and KRAS dosage define pancreatic cancer phenotypes.* Nature, 2018. **554**(7690): p. 62-68.
15. Chan-Seng-Yue, M., et al., *Transcription phenotypes of pancreatic cancer are driven by genomic events during tumor evolution.* Nat. Genet., 2020. **52**(2): p. 231-240.
16. *Explore the Cancer Dependency Map.*
17. Connor, A.A., et al., *Integration of Genomic and Transcriptional Features in Pancreatic Cancer Reveals Increased Cell Cycle Progression in Metastases.* Cancer Cell, 2019. **35**(2): p. 267-282.e7.
18. Somerville, T.D.D., et al., *TP63-Mediated Enhancer Reprogramming Drives the Squamous Subtype of Pancreatic Ductal Adenocarcinoma.* Cell Rep., 2018. **25**(7): p. 1741-1755.e7.
19. Hayashi, A., et al., *A unifying paradigm for transcriptional heterogeneity and squamous features in pancreatic ductal adenocarcinoma.* Nature Cancer, 2020. **1**(1): p. 59-74.
20. Oki, S., et al., *ChIP-Atlas: a data-mining suite powered by full integration of public ChIP-seq data.* EMBO Rep., 2018. **19**(12).
21. Collisson, E.A., et al., *Subtypes of pancreatic ductal adenocarcinoma and their differing responses to therapy.* Nat. Med., 2011. **17**(4): p. 500-503.
22. Roe, J.-S., et al., *Enhancer Reprogramming Promotes Pancreatic Cancer Metastasis.* Cell, 2017. **170**(5): p. 875-888.e20.
23. Wang, L., et al., *Oncogenic function of ATDC in pancreatic cancer through Wnt pathway activation and beta-catenin stabilization.* Cancer Cell, 2009. **15**(3): p. 207-219.
24. Somerville, T.D.D., et al., *ZBED2 is an antagonist of interferon regulatory factor 1 and modifies cell identity in pancreatic cancer.* Proc. Natl. Acad. Sci. U. S. A., 2020.
25. Lefebvre, C., et al., *A human B-cell interactome identifies MYB and FOXM1 as master regulators of proliferation in germinal centers.* Mol. Syst. Biol., 2010. **6**: p. 377.
26. Clauset, A., M.E.J. Newman, and C. Moore, *Finding community structure in very large networks.* Phys. Rev. E Stat. Nonlin. Soft Matter Phys., 2004. **70**(6 Pt 2): p. 066111.
27. Kirby, M.K., et al., *RNA sequencing of pancreatic adenocarcinoma tumors yields novel expression patterns associated with long-term survival and reveals a role for ANGPTL4.* Mol. Oncol., 2016. **10**(8): p. 1169-1182.

28. Alvarez, M.J., et al., *Functional characterization of somatic mutations in cancer using network-based inference of protein activity.* Nat. Genet., 2016. **48**(8): p. 838-847.
29. Moffitt, R.A., et al., *Virtual microdissection identifies distinct tumor- and stroma-specific subtypes of pancreatic ductal adenocarcinoma.* Nat. Genet., 2015. **47**(10): p. 1168-1178.
30. Pilarsky, C., et al., *Activation of Wnt signalling in stroma from pancreatic cancer identified by gene expression profiling.* J. Cell. Mol. Med., 2008. **12**(6B): p. 2823-2835.
31. Pei, H., et al., *FKBP51 affects cancer cell response to chemotherapy by negatively regulating Akt.* Cancer Cell, 2009. **16**(3): p. 259-266.
32. Yang, S., et al., *A Novel MIF Signaling Pathway Drives the Malignant Character of Pancreatic Cancer by Targeting NR3C2.* Cancer Res., 2016. **76**(13): p. 3838-3850.
33. Hiraoka, N., et al., *CXCL17 and ICAM2 are associated with a potential anti-tumor immune response in early intraepithelial stages of human pancreatic carcinogenesis.* Gastroenterology, 2011. **140**(1): p. 310-321.
34. Donahue, T.R., et al., *Integrative survival-based molecular profiling of human pancreatic cancer.* Clin. Cancer Res., 2012. **18**(5): p. 1352-1363.
35. Cancer Genome Atlas Research Network. Electronic address, a.a.d.h.e. and N. Cancer Genome Atlas Research, *Integrated Genomic Characterization of Pancreatic Ductal Adenocarcinoma.* Cancer Cell, 2017. **32**(2): p. 185-203.e13.
36. Puleo, F., et al., *Stratification of Pancreatic Ductal Adenocarcinomas Based on Tumor and Microenvironment Features.* Gastroenterology, 2018. **155**(6): p. 1999-2013.e3.
37. Bailey, P., et al., *Genomic analyses identify molecular subtypes of pancreatic cancer.* Nature, 2016. **531**(7592): p. 47-52.
38. The, G.C., *The Genotype-Tissue Expression (GTEx) pilot analysis: Multitissue gene regulation in humans.* Science, 2015. **348**(6235): p. 648-660.
39. Hoadley, K.A., et al., *Cell-of-Origin Patterns Dominate the Molecular Classification of 10,000 Tumors from 33 Types of Cancer.* Cell, 2018. **173**(2): p. 291-304.e6.
40. Ghandi, M., et al., *Next-generation characterization of the Cancer Cell Line Encyclopedia.* Nature, 2019. **569**(7757): p. 503-508.
41. Ying, H., et al., *Oncogenic Kras maintains pancreatic tumors through regulation of anabolic glucose metabolism.* Cell, 2012. **149**(3): p. 656-670.
42. Viale, A., et al., *Oncogene ablation-resistant pancreatic cancer cells depend on mitochondrial function.* Nature, 2014. **514**(7524): p. 628-632.
43. Sivakumar, S., et al., *Master Regulators of Oncogenic KRAS Response in Pancreatic Cancer: An Integrative Network Biology Analysis.* PLoS Med., 2017. **14**(1): p. e1002223.

44. Bryant, K.L., et al., *Combination of ERK and autophagy inhibition as a treatment approach for pancreatic cancer.* Nat. Med., 2019. **25**(4): p. 628-640.
45. Alvarez, M.J., et al., *A precision oncology approach to the pharmacological targeting of mechanistic dependencies in neuroendocrine tumors.* Nat. Genet., 2018. **50**(7): p. 979-989.
46. Mundi, P.S., et al., *Pre-clinical validation of an RNA-based precision oncology platform for patient-therapy alignment in a diverse set of human malignancies resistant to standard treatments.* bioRxiv, 2021: p. 2021.10.03.462951.
47. Kikuchi, H., et al., *Oncogenic KRAS and BRAF differentially regulate hypoxia-inducible factor-1alpha and -2alpha in colon cancer.* Cancer Res, 2009. **69**(21): p. 8499-506.
48. Olive, K.P., et al., *Inhibition of Hedgehog signaling enhances delivery of chemotherapy in a mouse model of pancreatic cancer.* Science, 2009. **324**(5933): p. 1457-61.
49. Hogenesch, J.B., et al., *The basic helix-loop-helix-PAS protein MOP9 is a brain-specific heterodimeric partner of circadian and hypoxia factors.* J. Neurosci., 2000. **20**(13): p. RC83.
50. Maemura, K., et al., *CLIF, a novel cycle-like factor, regulates the circadian oscillation of plasminogen activator inhibitor-1 gene expression.* J. Biol. Chem., 2000. **275**(47): p. 36847-36851.
51. Li, B., et al., *Fructose-1,6-bisphosphatase opposes renal carcinoma progression.* Nature, 2014. **513**(7517): p. 251-5.
52. Kwei, K.A., et al., *Genomic Profiling Identifies GATA6 as a Candidate Oncogene Amplified in Pancreatobiliary Cancer.* PLoS Genet., 2008. **4**(5): p. e1000081.
53. Fu, B., et al., *Frequent genomic copy number gain and overexpression of GATA-6 in pancreatic carcinoma.* Cancer Biol. Ther., 2008. **7**(10): p. 1593-1601.
54. Martinelli, P., et al., *GATA6 regulates EMT and tumour dissemination, and is a marker of response to adjuvant chemotherapy in pancreatic cancer.* Gut, 2017. **66**(9): p. 1665-1676.
55. Martinelli, P., et al., *The acinar regulator Gata6 suppresses KrasG12V-driven pancreatic tumorigenesis in mice.* Gut, 2016. **65**(3): p. 476-486.
56. Brady, J.J., et al., *An Arntl2-Driven Secretome Enables Lung Adenocarcinoma Metastatic Self-Sufficiency.* Cancer Cell, 2016. **29**(5): p. 697-710.
57. Mazzoccoli, G., et al., *ARNTL2 and SERPINE1: potential biomarkers for tumor aggressiveness in colorectal cancer.* J. Cancer Res. Clin. Oncol., 2012. **138**(3): p. 501-511.

58. Wang, Z., et al., *ARNTL2 promotes pancreatic ductal adenocarcinoma progression through TGF/BETA pathway and is regulated by miR-26a-5p.* Cell Death Dis., 2020. **11**(8): p. 692.
59. Miyabayashi, K., et al., *Intraductal Transplantation Models of Human Pancreatic Ductal Adenocarcinoma Reveal Progressive Transition of Molecular Subtypes.* Cancer Discov., 2020.
60. Maurer, H.C. and K.P. Olive, *Laser Capture Microdissection on Frozen Sections for Extraction of High-Quality Nucleic Acids.* Methods Mol. Biol., 2019. **1882**: p. 253-259.
61. Love, M.I., W. Huber, and S. Anders, *Moderated estimation of fold change and dispersion for RNA-seq data with DESeq2.* Genome Biol., 2014. **15**(12): p. 550.
62. Hu, H., et al., *AnimalTFDB 3.0: a comprehensive resource for annotation and prediction of animal transcription factors.* Nucleic Acids Res., 2019. **47**(D1): p. D33-D38.
63. Shannon, P., et al., *Cytoscape: a software environment for integrated models of biomolecular interaction networks.* Genome Res., 2003. **13**(11): p. 2498-2504.
64. Alvarez, M.J., F. Giorgi, and A. Califano, *Using viper, a package for Virtual Inference of Protein-activity by Enriched Regulon analysis.* Bioconductor, 2014: p. 1-14.
65. Subramanian, A., et al., *Gene set enrichment analysis: a knowledge-based approach for interpreting genome-wide expression profiles.* Proc. Natl. Acad. Sci. U. S. A., 2005. **102**(43): p. 15545-15550.
66. Ritchie, M.E., et al., *limma powers differential expression analyses for RNA-sequencing and microarray studies.* Nucleic Acids Res., 2015. **43**(7): p. e47.
67. Therneau, T.M. and P.M. Grambsch, *Modeling Survival Data: Extending the Cox Model*. Statistics for Biology and Health. 2013: Springer Science & Business Media. 350.
68. Viechtbauer, W., *Conducting Meta-Analyses in R with the metafor Package.* Journal of Statistical Software, Articles, 2010. **36**(3): p. 1-48.
69. Badgley, M.A., et al., *Cysteine depletion induces pancreatic tumor ferroptosis in mice.* Science, 2020. **368**(6486): p. 85-89.
70. The Cancer Genome Atlas Research, N., *PanCanAtlas Publications.*

Figure 1

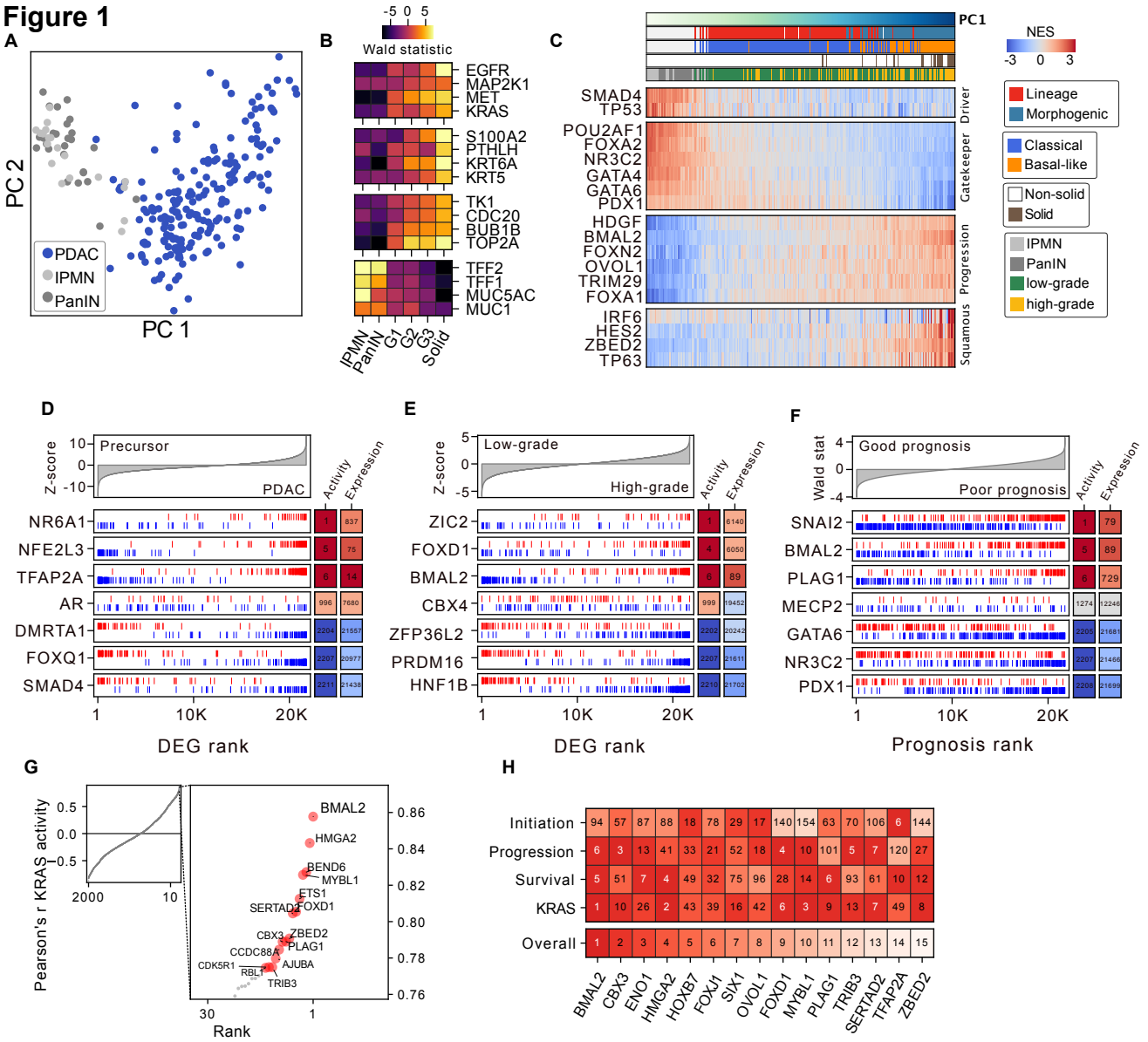
A
PC 2
PC 1
PDAC
IPMN
PanIN
B
Wald statistic
-5 0 5
EGFR
MAP2K1
MET
KRAS
S100A2
PTHLH
KRT6A
KRT5
TK1
CDC20
BUB1B
TOP2A
TFF2
TFF1
MUC5AC
MUC1
IPMN
PanIN
G1
G2
G3
Solid
C
PC1
NES
-3 0 3
SMAD4
TP53
Driver
POU2AF1
FOXA2
NR3C2
GATA4
GATA6
PDX1
Gatekeeper
HDGF
BMAL2
FOXN2
OVOL1
TRIM29
FOXA1
Progression
IRF6
HES2
ZBED2
TP63
Squamous
Lineage
Morphogenic
Classical
Basal-like
Non-solid
Solid
IPMN
PanIN
low-grade
high-grade
D
Z-score
Precursor
PDAC
Activity
Expression
NR6A1
NFE2L3
TFAP2A
AR
DMRTA1
FOXQ1
SMAD4
DEG rank
E
Low-grade
High-grade
ZIC2
FOXD1
BMAL2
CBX4
ZFP36L2
PRDM16
HNF1B
DEG rank
F
Wald stat
Good prognosis
Poor prognosis
SNAI2
BMAL2
PLAG1
MECP2
GATA6
NR3C2
PDX1
Prognosis rank
G
Pearson's r KRAS activity
Rank
BMAL2
HMGA2
BEND6
MYBL1
ETS1
SERTAD2
FOXD1
CBX3
ZBED2
CCDC88A
PLAG1
CDK5R1
AJUBA
RBL1
TRIB3
H
Initiation
Progression
Survival
KRAS
Overall
BMAL2
CBX3
ENO1
HMGA2
HOXB7
FOXJ1
SIX1
OVOL1
FOXD1
MYBL1
PLAG1
TRIB3
SERTAD2
TFAP2A
ZBED2

Figure 2

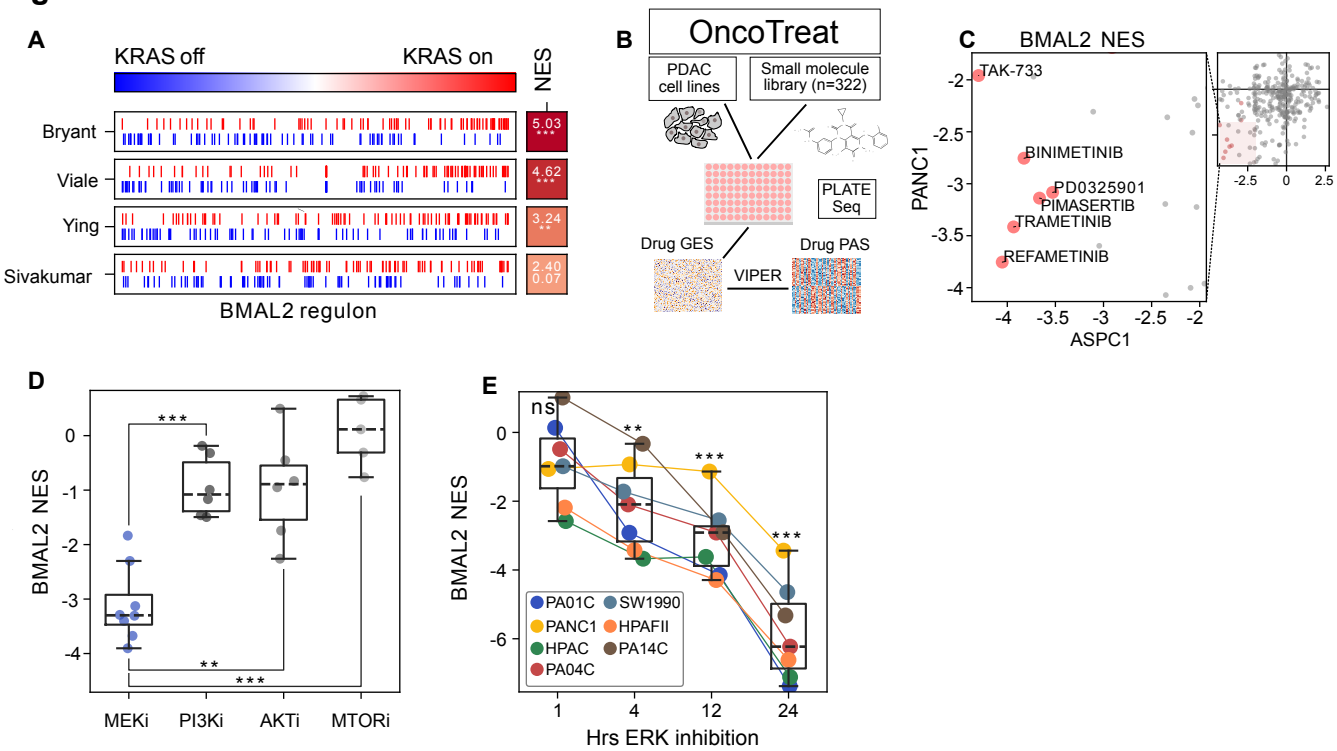
A
KRAS off
KRAS on
NES
Bryant
Viale
Ying
Sivakumar
5.03
4.62
3.24
2.40
0.07
BMAL2 regulon
B
OncoTreat
PDAC cell lines
Small molecule library (n=322)
PLATE Seq
Drug GES
Drug PAS
VIPER
C
BMAL2 NES
TAK-733
BINIMETINIB
PD0325901
PIMASERTIB
TRAMETINIB
REFAMETINIB
PANC1
ASPC1
D
BMAL2 NES
MEKi
PI3Ki
AKTi
MTORi
E
BMAL2 NES
ns
PA01C
SW1990
PANC1
HPAFII
HPAC
PA14C
PA04C
Hrs ERK inhibition

Figure 3

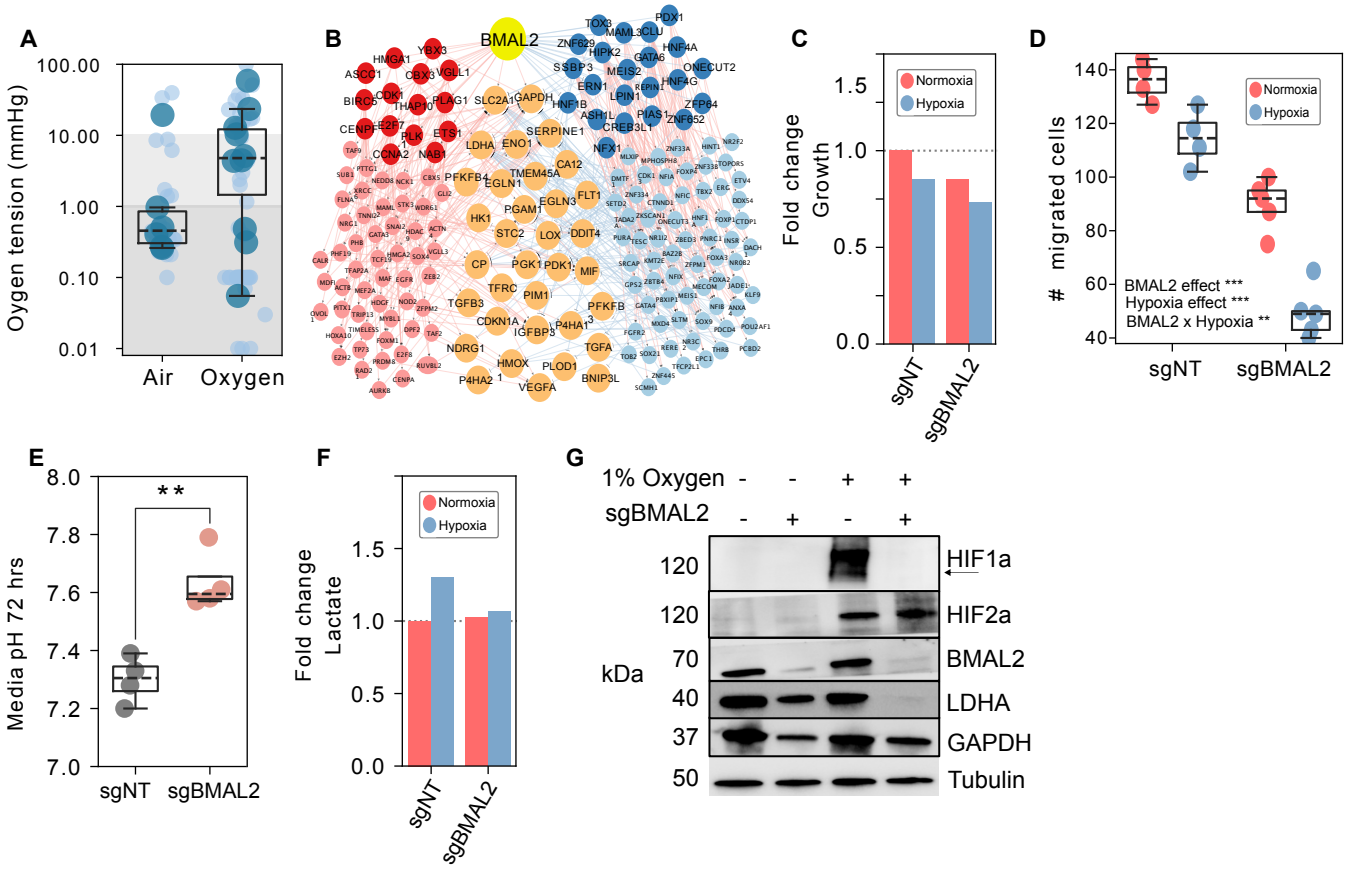
A
Oygen tension (mmHg)
100.00
10.00
1.00
0.10
0.01
Air
Oxygen
B
BMAL2
C
Fold change Growth
Normoxia
Hypoxia
1.5
1.0
0.5
0.0
sgNT
sgBMAL2
D
migrated cells
Normoxia
Hypoxia
BMAL2 effect ***
Hypoxia effect ***
BMAL2 x Hypoxia **
sgNT
sgBMAL2
E
Media pH 72 hrs
8.0
7.8
7.6
7.4
7.2
7.0
**
sgNT
sgBMAL2
F
Fold change Lactate
Normoxia
Hypoxia
1.5
1.0
0.5
0.0
sgNT
sgBMAL2
G
1% Oxygen - - + +
sgBMAL2 - + - +
kDa
120
120
70
40
37
50
HIF1a
HIF2a
BMAL2
LDHA
GAPDH
Tubulin